

Unstable Baroclinic Waves beyond Quasigeostrophic Theory

RICHARD ROTUNNO

National Center for Atmospheric Research, Boulder, Colorado*

DAVID J. MURAKI

Courant Institute, New York University, New York, New York

CHRIS SNYDER

National Center for Atmospheric Research, Boulder, Colorado*

(Manuscript received 11 March 1999, in final form 29 November 1999)

ABSTRACT

Quasigeostrophic theory is an approximation of the primitive equations in which the dynamics of geostrophically balanced motions are described by the advection of potential vorticity. Quasigeostrophic theory also represents a leading-order theory in the sense that it is derivable from the primitive equations in the asymptotic limit of zero Rossby number. Building upon quasigeostrophic theory, and the centrality of potential vorticity, the authors have recently developed a systematic asymptotic framework from which balanced, next-order corrections in Rossby number can be obtained. The approach is illustrated here through numerical solutions pertaining to unstable waves on baroclinic jets. The numerical solutions using the full primitive equations compare well with numerical solutions to our equations with accuracy one order beyond quasigeostrophic theory; in particular, the inherent asymmetry between cyclones and anticyclones is captured. Explanations of the latter and the associated asymmetry of the warm and cold fronts are given using simple extensions of quasigeostrophic-potential-vorticity thinking to next order.

1. Introduction

Quasigeostrophic theory is the foundation of our understanding of midlatitude weather disturbances as it offers a coherent and relatively simple explanation for their origin and synoptic-scale structure. A theory for the mesoscale structure of these disturbances has been more elusive as critical aspects of such mesoscale structure are almost certainly due to effects neglected in quasigeostrophic (QG) theory. The present authors (Muraki et al. 1999, hereinafter MSR) have recently developed a method to extend QG theory to higher powers in Rossby number while retaining its conceptual simplicity. In the present paper we show how our QG theory extended by one power in Rossby number (QG^{+1}) can be used as a framework for understanding certain mesoscale aspects of unstable baroclinic waves.

From the earliest primitive-equation (PE) numerical simulations of growing baroclinic waves onward, it has been noted that, relative to QG, there is a cyclonic bias in PE (Mudrick 1974; Snyder et al. 1991). The PE solutions suggest that the deviations from QG are balanced (i.e., not due to gravity waves) and this has in part motivated the use of models that attempt to extend the validity of QG. In one of the earliest attempts to go beyond QG in the study of finite-amplitude baroclinic waves, Hoskins and West (1979) presented solutions of the semigeostrophic equations (SG, Hoskins 1975) for baroclinic waves growing on a constant-potential-vorticity jet. Snyder et al. (1991) compared the latter simulations against their PE counterparts and found rather significant differences (see their Fig. 4), especially with respect to the nature of asymmetries between cyclones and anticyclones, and the placement of the fronts in the wave.

Other extended-regime models are far more accurate than SG in the simulation of unstable baroclinic waves (Allen et al. 1990; Allen and Newberger 1993; Whitaker 1993). However, the promise of SG was not only that one can get to higher levels of accuracy, but more important, the mathematical structure of SG retained the immense conceptual simplifications of QG theory ex-

* The National Center for Atmospheric Research is sponsored by the National Science Foundation.

Corresponding author address: R. Rotunno, NCAR, P.O. Box 3000, Boulder, CO 80307.
E-mail: rotunno@ncar.ucar.edu

pressed as the conservation and inversion of potential vorticity (PV). It was shown in MSR that QG^{+1} retains those same conceptual simplifications—here we show that QG^{+1} is also accurate enough to capture the major features of interest in the finite-amplitude baroclinic wave. For these reasons, we hope to convince the reader that QG^{+1} is the model that extends QGPV thinking [in the words of Hoskins et al. (1985)] to higher order. (See MSR for more detail on the relation between QG^{+1} and other extended-regime models.)

The plan of this work is as follows. In section 2 we write down the QG^{+1} equations and outline a method for their numerical solution. In section 3 we present numerical solutions of the QG^{+1} equations for growing waves on a constant-PV base-state jet. The QG^{+1} solutions are shown to compare well against companion PE solutions using the same initial condition. In particular, the QG^{+1} solutions accurately capture the nature of the asymmetries between cyclones and anticyclones. An analysis of these asymmetries is made in section 4. This analysis also provides a vehicle for showing how the many familiar analytical concepts of QG carry over to QG^{+1} as well as the new elements that are essential to explain the cyclonic bias in PE, and other features outside of QG. Conclusions and outlook are given in section 5.

2. QG^{+1} equations and solution technique

The perturbation theory developed in MSR is based on the inviscid, adiabatic, Boussinesq, hydrostatic equations of motion on an f plane written in a form called “ QG^{+1} ” (section 3 of MSR). Attention is restricted here to a fluid with constant rest-state stratification and bounded vertically by level surfaces.

The fundamental prognostic equation in QG^{+1} is the advection of disturbance potential vorticity q and disturbance potential temperature θ at the boundaries located at $z = s$; that is,

$$\mathcal{D}q = 0, \quad (\mathcal{D}\theta)^s = 0, \tag{1}$$

where

$$\mathcal{D} \equiv \frac{\partial}{\partial t} + u \frac{\partial}{\partial x} + v \frac{\partial}{\partial y} + \epsilon w \frac{\partial}{\partial z}, \tag{2}$$

and ϵ is the Rossby number. A key step in the development of the QG^{+1} system is the representation of the horizontal velocity components u and v , and θ in terms of the potentials Φ , F , and G , namely,

$$\begin{pmatrix} v \\ -u \\ \theta \end{pmatrix} = \nabla\Phi + \nabla \times \begin{pmatrix} F \\ G \\ 0 \end{pmatrix} = \begin{pmatrix} \Phi_x - G_z \\ \Phi_y + F_z \\ \Phi_z + G_x - F_y \end{pmatrix}. \tag{3}$$

Using continuity, the vertical velocity w may be expressed as

$$\epsilon w = F_x + G_y. \tag{4}$$

The QG^{+1} system is (1)–(4), along with MSR’s (28)–(29), which are prognostic equations for F and G [and which in the small- ϵ approximation allow the inversion of (q, θ^s) for Φ , F , and G]. This set is an exact form of the PE. In the QG^{+1} system, QG emerges as the leading-order theory by setting $\epsilon = 0$; here we examine a theory with one order of accuracy in ϵ beyond QG (QG^{+1}). In section 4b of MSR it was shown that the inversion of q for Φ is through solution of

$$\begin{aligned} \nabla^2\Phi + \epsilon[(\Phi_{xx} + \Phi_{yy})\Phi_{zz} - \Phi_{xz}\Phi_{xz} - \Phi_{yz}\Phi_{yz}] \\ = q + O(\epsilon^2), \quad (\Phi_z + G_x - F_y)^s = \theta^s. \end{aligned} \tag{5}$$

At the level bounding surfaces, $(F_x + G_y)^s = 0$ by (4), and without loss of generality we can choose $F^s = G^s = 0$ for computational convenience. The equations for F and G from section 4b of MSR are

$$\nabla^2 F = 2\epsilon J(\Phi_z, \Phi_x) + O(\epsilon^2), \quad F^s = 0 \quad \text{and} \tag{6}$$

$$\nabla^2 G = 2\epsilon J(\Phi_z, \Phi_y) + O(\epsilon^2), \quad G^s = 0, \tag{7}$$

respectively, and $J(f, g) \equiv f_x g_y - f_y g_x$. Once Φ has been obtained from the solution of (5), (F, G) can be obtained through the solution of (6), (7). With Φ , F , and G we can construct through (3), (4) the (u, v, w) needed to evolve (q, θ^s) .

The potential Φ differs from the perturbation pressure ϕ by an amount determined by the solution of

$$\begin{aligned} \nabla^2(\phi - \Phi) = 2\epsilon J(\Phi_x, \Phi_y) + O(\epsilon^2), \\ (\phi - \Phi)_z^s = 0, \end{aligned} \tag{8}$$

where we have used $F^s = G^s = 0$ in the boundary condition. [Equation (8) derives from (33) of MSR after correction of a typographical sign error in the latter.] Note that ϕ is not required in the solution cycle described above, but may be computed as desired through (8).

To summarize the QG^{+1} solution recipe:

- 1) Given initial values (q, θ^s) , invert for Φ by (5).
- 2) Obtain (F, G) from (6)–(7).
- 3) Advance (q, θ^s) to the next time level through (1).

This method for solving QG^{+1} is exactly parallel to that used in solving the QG equations expressed in the form of the conservation of QGPV and its inversion. With $\epsilon = 0$, they are the same. Thus such an existing QG model can immediately be extended to QG^{+1} accuracy by the addition of one extra iteration of (5) to correct Φ for the $O(\epsilon)$ term, and the solution of (6), (7), amounting to three extra Poisson-equation solutions per time step. The numerical solution method is described in detail in the appendix.

Being an asymptotic theory, QG^{+1} builds an extra layer of accuracy on QG theory, and so an attractive feature of QG^{+1} is that it is composed of familiar elements from QG theory. QG^{+1} PV is materially conserved and may be inverted for the flow. The rhs of inversion equations (6), (7) are, respectively, the x and

y components of the \mathbf{Q} vector (Hoskins et al. 1978) to leading order in ϵ . Finally, as in QG, the QG^{+1} PV inversion equation (5) is second order in the single potential (Φ); further analysis of (5) is given in section 4.

3. Unstable baroclinic waves in QG^{+1}

a. Base state

Simulations of baroclinic waves growing on a zonal baroclinic jet provide the test bed for the QG^{+1} model. Arguably the simplest meteorologically relevant jet is one of constant interior PV with jet strength concentrated at central latitude $y = 0$. Thus we look for an x -independent solution $\bar{\Phi}$ of (5) with \bar{q} constant on the domain $-Y/2 \leq y \leq +Y/2$ and $0 \leq z \leq 1$; neglecting terms of $O(\epsilon^2)$, (5) becomes

$$\begin{aligned} \bar{\Phi}_{yy} + \bar{\Phi}_{zz} + \epsilon(\bar{\Phi}_{yy}\bar{\Phi}_{zz} - \bar{\Phi}_{yz}\bar{\Phi}_{yz}) &= \bar{q}, \\ (\bar{\Phi}_z)_s &= \bar{\theta}^s, \end{aligned} \quad (9)$$

where now the script s denotes boundary values at $z = 0, 1$. The x independence of $\bar{\Phi}$ implies through (6), (7) that $\bar{F} = \bar{G} = 0$. Pursuing a strategy similar in concept to that used by Hoskins and West (1979), we let

$$\begin{aligned} \bar{\Phi}(y, z) &= Ay^2 - \frac{1}{2}yz(2 - \mu) + \tilde{\Phi}(y, z), \\ \bar{\theta}^s &= -\frac{1}{2}y(2 - \mu) + \tilde{\theta}^s, \\ \bar{q} &= A - \frac{\epsilon}{4}(2 - \mu)^2, \end{aligned} \quad (10)$$

where the functions with tildes are periodic over distance Y . Substituting (10) into (9), we obtain

$$\begin{aligned} \tilde{\Phi}_{yy} + \tilde{\Phi}_{zz} + \epsilon(\tilde{\Phi}_{yy}\tilde{\Phi}_{zz} - \tilde{\Phi}_{yz}\tilde{\Phi}_{yz}) + (2 - \mu)\tilde{\Phi}_{yz} + A\tilde{\Phi}_{zz} \\ = 0, \end{aligned} \quad (11)$$

with boundary conditions given by

$$\tilde{\theta}^1 = \frac{\mu}{2} \frac{\sin ly}{\tanh l}, \quad \tilde{\Phi}^0 = 0, \quad (12)$$

where instead of specifying $\tilde{\theta}^0$, we require for simplicity no flow at $z = 0$; the form of (12) is motivated by the QG constant-PV jet $\bar{u} = -2Ay + z(1 - \mu/2) + (\mu/2)(\sinh lz / \sinh l) \cos ly$, where $l = 2\pi/Y$. Figure 1 displays $\bar{u}(y, z)$ and full potential temperature $z/\epsilon + \bar{\theta}(y, z)$ for $Y = 5.53$, $\epsilon = 0.3$, $A = 0$, and $\mu = 1$. The numerical solution of (11), (12) is described in the appendix.

b. Simulations of unstable baroclinic waves in PE, QG^{+1} , and QG

The QG^{+1} Eqs. (1)–(8) are now solved numerically for horizontally periodic perturbations (denoted by primed quantities) away from the base state (10), as described in detail in the appendix. The QG^{+1} model is

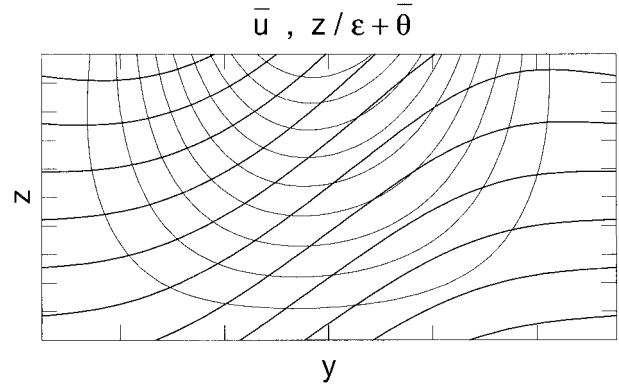


FIG. 1. Base-state jet $\bar{u}(y, z)$ (thin lines, c.i. = 0.1) and total potential temperature $z/\epsilon + \bar{\theta}(y, z)$ (thick lines, c.i. = 0.553) calculated from (10) with $\mu = 1$ and $\epsilon = 0.3$. Tick marks separated by one nondimensional unit.

initialized with an unstable normal mode (discussed below) with zonal wavelength $X = 4$ and scaled so that $|\theta'(z = 0)|_{\max} = 0.15$. We restrict attention here to cases where q is constant in order to retain the considerable conceptual and computational simplification of having all the time evolution embodied in advection of boundary θ . The QG^{+1} base state and normal mode is also used as the initial condition for a companion PE integration, which is done with the same spatial resolution as the QG^{+1} model, no spatial filters, and a weak time filter [coefficient = 0.05; see section 3b of Snyder et al. (1991)].

The first two columns of Fig. 2 compare PE and QG^{+1} boundary θ and pressure perturbation ϕ' at $t = 10$ for a case corresponding to the base-state jet shown in Fig. 1 ($\mu = 1$, $A = 0$, $\epsilon = 0.3$); the third column shows for reference the QG solution, which is initialized with the QG base state ($\mu = 1$, $A = 0$, $\epsilon = 0$) and normal mode. At $z = 0$, QG^{+1} captures the tendency, absent in QG, for the narrow warm tongue (W in Fig. 2d) to be wrapped cyclonically into the low, while the broad cold air mass (C in Fig. 2d) extends in an arc between the high and the low. The QG^{+1} model also captures the upper-level frontogenesis occurring west of the upper pressure trough (UF in Fig. 2a). The somewhat stronger features in the QG^{+1} model are due to the fact that the QG^{+1} mode grows faster (see below) than the PE mode; comparing the PE solution at $t = 11$ (not shown) with the QG^{+1} solution at $t = 10$ indicates a very close correspondence between the solutions. At both $z = 0$ (surf) and $z = 1$ (lid) the QG^{+1} model captures the high/low asymmetry in ϕ' .

The example shown in Figs. 1 and 2 for $\epsilon = 0.3$ is almost certainly outside the range of asymptotic validity of the QG^{+1} equations, as is the time length of the run $t = O(1/\epsilon)$. Asymptotic agreement between PE and QG^{+1} can be demonstrated for smaller ϵ (see below). The point we wish to make in this section is that QG^{+1} can be profitably used to simulate mesoscale structure

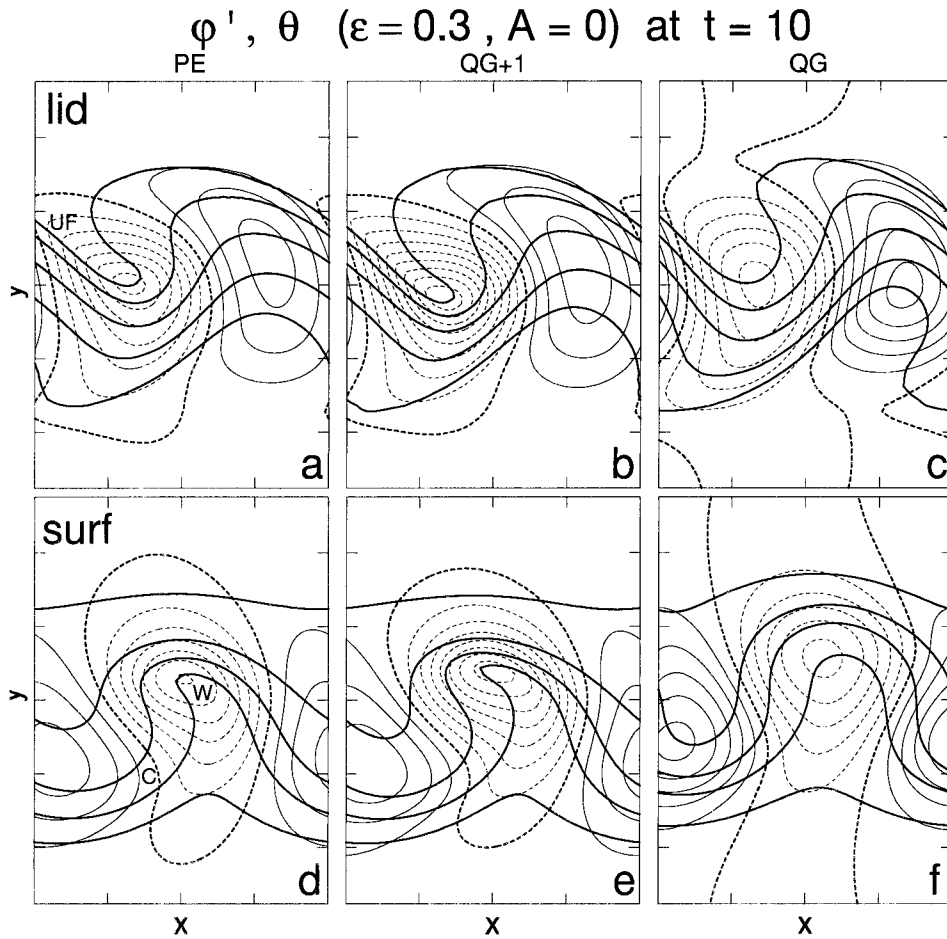


FIG. 2. Comparison of perturbation pressure ϕ' (thin lines, c.i. = 0.1; here and throughout negatives values are indicated by dashed lines and the zero value is denoted by the thick dashed line) and potential temperature θ (thick solid lines, c.i. = 0.553) from the QG⁺¹ and PE models initialized with the base-state jet of Fig. 1 plus a normal-mode perturbation. Also shown for reference is a QG integration initialized with a normal mode and base state obtained from (10)–(12) with $\mu = 1$, $\epsilon = 0$, and $A = 0$. Tick marks separated by one nondimensional unit.

for meteorologically relevant parameter settings. In section 4 we show how the QG⁺¹ equations may be used to analyze that mesoscale structure.

c. Error analysis of QG⁺¹

Within the range of asymptotic validity of QG⁺¹, any difference between the PE and QG⁺¹ solutions should vary in proportion to ϵ^2 . For example, we have checked that the difference in growth rate between the PE and QG⁺¹ unstable modes increases as $a\epsilon^2$, where a is a constant of proportionality. A different QG⁺¹ solution technique may produce a different a for different solution features, but does not change the fundamental fact that $O(\epsilon^2)$ differences between PE and QG⁺¹ are to be expected. Recent results on linear baroclinic instability in extended-regime models may be found in Smith and Vallis (1999).

To establish the accuracy of the present numerical

QG⁺¹ solutions, we did the following. Taking $\mu = A = 0$ in (10)–(12), the Eady base state is recovered; the QG⁺¹ model is then initialized with the small-amplitude semigeostrophic Eady wave (Hoskins 1975), namely,

$$\begin{aligned}
 q' &= 0, \\
 \theta'^s(x, y) &= \sqrt{\lambda} \sin l(y - \epsilon s) \\
 &\quad \times (\hat{A} \sin kx \sinh \sqrt{\lambda} s + \hat{B} \cos kx \cosh \sqrt{\lambda} s), \\
 \hat{A} &= \hat{\Phi} \sqrt{\frac{\lambda}{2} \coth \frac{\lambda}{2} - 1}, \\
 \hat{B} &= \hat{\Phi} \sqrt{1 - \frac{\lambda}{2} \tanh \frac{\lambda}{2}},
 \end{aligned} \tag{13}$$

where now $s = \pm 1/2$ and $\lambda \equiv \sqrt{k^2 + l^2}$. In the present test we consider the square wave $k = l = 2\pi/5.53$ (for maximum growth rate), and $\hat{\Phi} = 0.1$. The PE model is

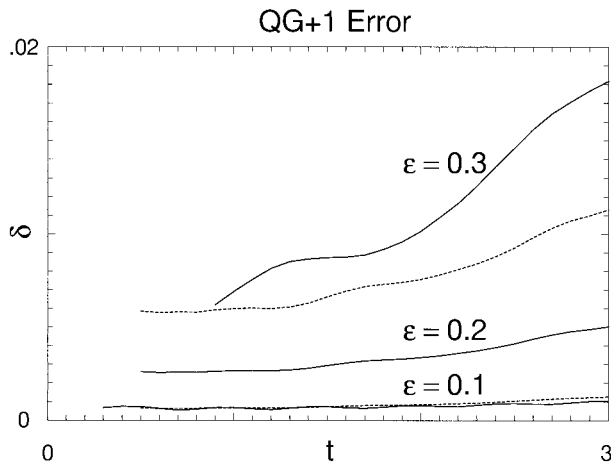


FIG. 3. Error $\delta(t; \epsilon)$ as defined in (14) (solid lines). The two dashed lines represent $(1/4)\delta(t; \epsilon = 0.2)$ and $(1/4)\delta(t; \epsilon = 0.2)$.

initialized with the velocity, pressure, and potential temperature produced after one solution cycle of the QG⁺ model. The error is measured by

$$\delta(t; \epsilon) = \frac{\sum (v_{PE} - v_{QG^+})^2}{\sum v_{PE}^2}, \quad (14)$$

where the summation is over the entire domain; computation of δ was done for $\epsilon = 0.1, 0.2, 0.3$. In addition to the systematic error growth, we observed an internal wave in the PE model that produces a time oscillation in $\delta(t; \epsilon)$ with dimensional period approximately 2×10^5 s. Hence shown in Fig. 3 is $\tau^{-1} \int_{t-\tau/2}^{t+\tau/2} \delta(t'; \epsilon) dt'$, where τ corresponds to a dimensional time of 2×10^5 s for each ϵ . Also shown as dashed lines in Fig. 3 are curves $(1/4)\delta(t; 0.2)$ and $(1/4)\delta(t; 0.2)$; the latter curves indicate that δ is proportional to ϵ^2 in the range $\epsilon < 0.2$, while for larger ϵ the scaling is beginning to break down.

4. QG⁺ analysis

Figure 2 illustrates in an obvious way the nature of the QG⁺ equations. As the first approximation to PE, QG gives the basic mechanism of wave growth (i.e., baroclinic instability) and the synoptic-scale structure (e.g., westward phase tilt with height of ϕ'). In the next approximation, QG⁺ retains the basic QG structure and adds mesoscale structure, the most obvious being the asymmetry between cyclones and anticyclones, and between warm and cold fronts. In this section we show how the QG⁺ equations provide a framework for understanding these added features.

a. The asymmetry between cyclones and anticyclones

The difference between cyclones and anticyclones is described in many textbooks as a consequence of the gradient wind law, $r^{-1}V^2 + fV = P_r$, where r is the

radius in cylindrical coordinates, V is the azimuthal velocity, P is pressure (density has been set to one), and f is the Coriolis parameter. Given a cyclone ($V > 0$) and an anticyclone ($V < 0$) of equal wind magnitude, the gradient wind law says that the pressure gradient is stronger in the cyclone than it is in the anticyclone. However, because we desire an explanation from first principles, V cannot be considered as a given [in other words, the gradient wind law is one steady-state equation in two unknowns (V, P)]. At a deeper level, in the QG⁺ system, it is the potential Φ that is the dynamically important quantity, and the pressure ϕ enters only diagnostically through (8). To illustrate these points, consider the barotropic vortex flow $\Phi = \omega(x^2 + y^2)/2 = \omega r^2/2$, $F = G = 0$, which is a solution to the QG⁺ equations with $q = \omega$; with the latter solution, (8) gives $\phi_r = (\omega + \epsilon\omega^2)r$, which is the gradient wind law for a vortex in solid-body rotation. To make a deductive argument for the difference in ϕ_r between cyclones and anticyclones, one needs a theory for the difference in ω , that is to say Φ , that evolves between cyclones and anticyclones in a growing baroclinic wave. Hence one needs to look into the dynamical evolution of Φ .

The first two columns of Fig. 4 depict the most-unstable-normal-mode initial condition for the simulation shown in Fig. 2 in terms of Φ' and the divergent velocity ($-F_z, -G_z$).¹ The mode is obtained by integrating the linearized QG⁺ equations forward until a constant growth rate and modal shape was assumed (20 time units); initial conditions for that integration were (13) except $\sin l(y - \epsilon s)$ was replaced with $\exp[-(y - \epsilon s)^2 / (0.1Y)^2]$; $X = 4$, $Y = 5.53$, and $\hat{\Phi} = 0.001$. We note in passing that the modal structure of Φ' is similar to that of ϕ' found in PE calculations of normal modes of the Hoskins and West (1979) jet by Snyder et al. (1991) as it tilts northward as well as westward with height, and has a northwest-southeast phase tilt in a horizontal plane. The structure of the divergent wind ($-F_z, -G_z$) is just what one expects based on the QG concept of \mathbf{Q} vectors [see Fig. 2 of Hoskins et al. (1978)]. Substituting $\Phi = \Phi_0 + O(\epsilon)$ into (6), (7) shows that the rhs are precisely Q^x and Q^y , respectively, as noted in section 2.

The linear mode is used as the initial condition for the nonlinear QG⁺ model and we have observed that there is an immediate high/low bias produced in Φ' . The origin of the Φ' asymmetry can be traced to the nonlinear terms in PV inversion (5). The nonlinear contribution Φ'_{nl} to the PV inversion for $\Phi'(t = 0)$, as defined by the solution of (A3) forced by the nonlinear terms and with homogeneous boundary conditions, is shown in the third column of Fig. 4, and is such that lows of $\Phi'(t = 0)$ (not shown) are enhanced relative to

¹ Since the velocity associated with Φ is nondivergent, divergence is uniquely associated with $(-F_z, -G_z)$. Note, however, that the velocity associated with F and G can also have a rotational component.

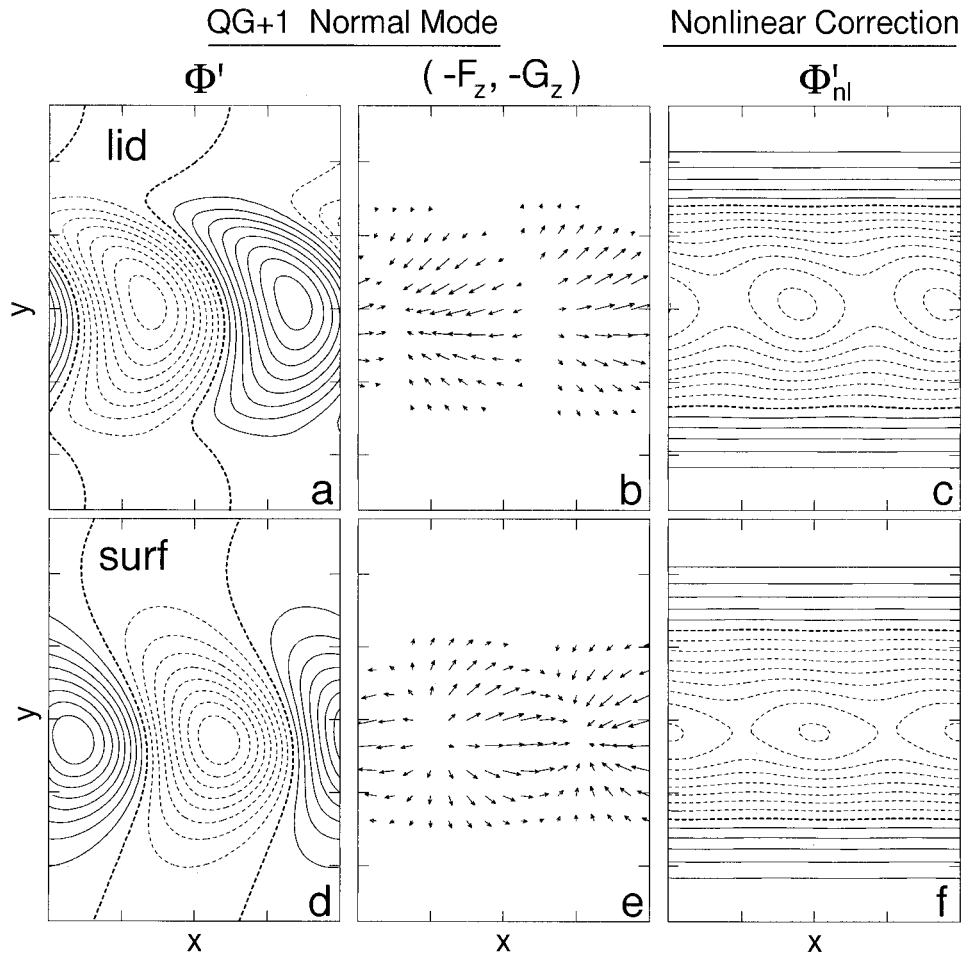


FIG. 4. Most unstable normal mode of the QG⁺ base state shown in Fig. 1 (a, b, d, e) and first adjustment in nonlinear QG⁺ simulations (c, f). Mode is depicted through Φ' (c.i. = 0.008) and $(-F_z, -G_z)$ (maximum vector length = 0.0226, vectors with length shorter than 0.2× the maximum are not plotted). The nonlinear correction Φ'_{nl} (c.i. = 0.0005) is produced in the inversion of the initial (q', θ') given by the normal mode.

highs. This biasing effect of Φ'_{nl} persists well into the large-amplitude phase. The high-low asymmetry in Φ' is plainly evident at $t = 5$ (first column of Fig. 5), as is the fact that Φ'_{nl} (third column of Fig. 5) is to favor the lows and disfavor the highs.

A simple demonstration of the effect of the nonlinear $O(\epsilon)$ corrections in (5) can be obtained by considering the Eady edge wave as a crude model for the mode Φ^m , that is, let

$$\Phi^m = \hat{A} \sin ly \sin kx \exp(-\sqrt{k^2 + l^2}z). \quad (15)$$

The nonlinear correction to $\Phi'(t = 0)$ appears as the PV anomaly

$$\begin{aligned} & \Phi^m_{xz} \Phi^m_{xz} + \Phi^m_{yz} \Phi^m_{yz} - (\Phi^m_{xt} + \Phi^m_{yy}) \Phi^m_{zz} \\ &= \hat{A}^2 k^2 (k^2 + l^2) [\sin^2 ly + (l/k)^2 \sin^2 kx] \\ & \times \exp(-2\sqrt{k^2 + l^2}z). \end{aligned} \quad (16)$$

Equation (16) indicates that the forcing of nonlinear corrections to Φ' has the form of a positive PV anomaly

with maxima at $ly = \pi/2, kx = \pi/2, 3\pi/2$; for $(l/k)^2 \ll 1$ (as in the present case), the pattern implied for Φ'_{nl} by (16) is much like what the numerical solutions show in Figs. 4, 5.

The cyclonic bias demonstrated in (16) is of a general nature. Using the nondimensionalization of MSR, the PV is

$$Q = (\mathbf{k} + \epsilon \boldsymbol{\omega}) \cdot (\mathbf{k} + \epsilon \nabla \theta), \quad (17)$$

where $\boldsymbol{\omega} = (\xi, \eta, \zeta) = (-v_z, u_z, v_x - u_y)$ is the vorticity in the hydrostatic approximation. In the reference state, $Q = 1$; other states with the same Q must by (17) satisfy

$$(\zeta + \theta_z) + \epsilon \boldsymbol{\omega} \cdot \nabla \theta = 0, \quad (18)$$

where a factor of ϵ has been canceled. With $\epsilon = 0$ in (18), the QG result $\zeta + \theta_z = 0$ is recovered; this together with the thermal wind relation implies

$$\boldsymbol{\omega} = -\nabla \theta. \quad (19)$$

Denoting QG results with the subscript “0,” and corrections with subscript “1,” (18) with (19) gives

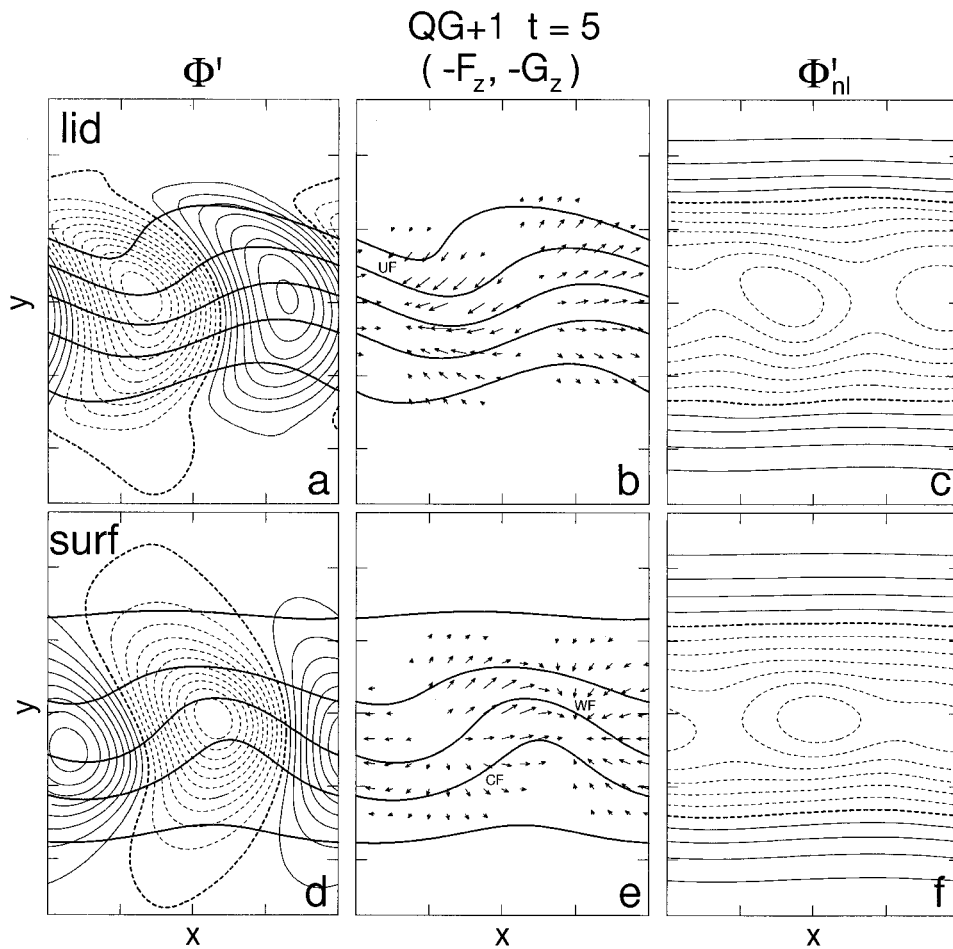


FIG. 5. As in Fig. 4 except at $t = 5$ and with different contour intervals (c.i. = 0.02 for Φ' , c.i. = 0.005 for Φ'_{nl} , and the maximum vector length = 0.0935).

$$\zeta_1 + \theta_{1z} = -\omega_0 \cdot \nabla \theta_0 = \omega_0 \cdot \omega_0 > 0. \quad (20) \quad b. \text{ The roles of } \Phi, F, \text{ and } G$$

Hence at next order in ϵ there is always a correction to the QGPV ($\zeta_0 + \theta_{0z}$) that is a positive anomaly in the vicinity of a localized QG disturbance. The expression of the velocity field through (3) allows this PV correction to be expressed as a correction in the single potential Φ .

Before leaving this section, we note that the cyclonic bias in PE simulations of baroclinic waves is sometimes attributed to the stretching of the vertical component of relative vorticity (Polavarapu and Peltier, 1990; Rotunno et al. 1994; Garnier et al. 1998). The foregoing analysis shows, however, that all three components of vorticity contribute equally to the cyclonic bias in PV. Moreover, including stretching of relative vorticity in a dynamical model does not guarantee that the correct asymmetry between cyclones and anticyclones will be captured; for example, stretching is included in SG, but SG solutions for baroclinic waves do not produce the correct asymmetry (see Fig. 4 of Snyder et al. 1991).

The respective roles of Φ , F , and G in the evolution of the flow may be viewed through examination of the boundary-temperature advection. Figures 6a,b shows that, as expected for a growing baroclinic wave, the temperature perturbation and the advective temperature change are positively correlated. Figure 6c indicates that the velocity associated with the nondivergent ($-\Phi_y, \Phi_x$) wind is mostly responsible for the amplification of the baroclinic wave. Figures 6d and 5e indicate that the divergent wind ($-F_z, -G_z$) reinforces the frontogenesis produced by the nondivergent wind along the incipient surface warm front (WF in Fig. 5e) located near the low, and the incipient surface cold front (CF in Fig. 5e), which extends in an arc between the low and the high. Similar remarks can be made about the incipient upper front (UF in Fig. 5b) shown in Figs. 5a,b. Thus these solutions of the QG⁺ equations are consistent with the Hoskins and Bretherton (1972) view of frontogenesis as a process wherein the divergent wind positively re-

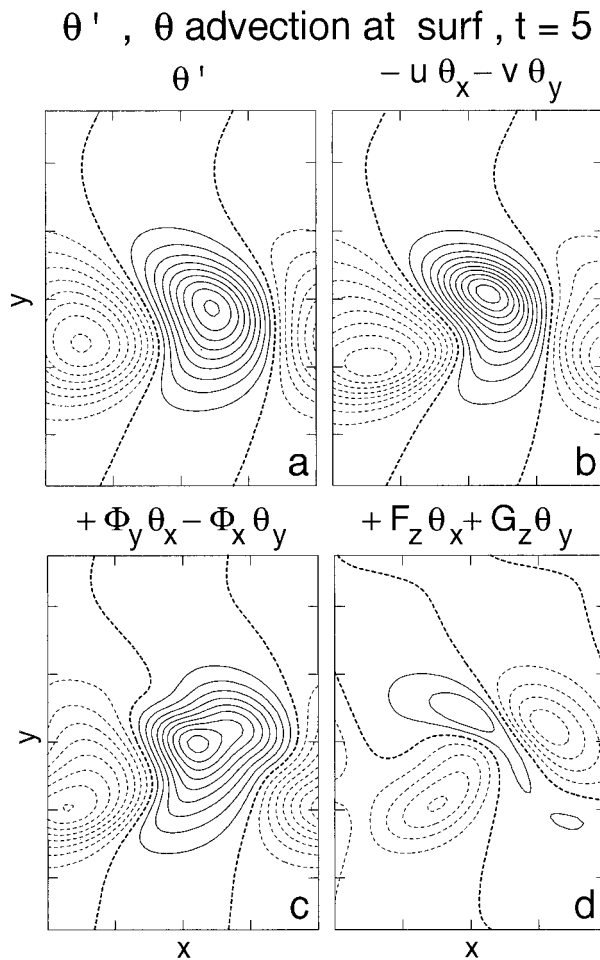


FIG. 6. (a) Surface θ' (c.i. = 0.05), (b) surface advection of θ by the full wind, (c) by the nondivergent (Φ) wind, and (d) by the divergent ($-F_z, -G_z$) wind at $t = 5$; c.i. = 0.01 for the advection fields.

inforces nondivergent-wind-produced frontogenesis. The large-scale asymmetry in the nondivergent wind (i.e., in Φ' ; Fig. 5d), produces a different distribution between warm-front- and cold-front-associated divergent wind fields (Fig. 5e), and accounts for their different structure (Rotunno et al. 1994; cf. Figs. 4, 5 with their Figs. 3, 4).

c. Other sources of asymmetry

Until now we have restricted the discussion to asymmetries that arise at a finite Rossby number. Another way asymmetry may develop is through the action of barotropic shear in the base state [represented by the term Ay^2 in (10); see Davies et al. 1991; Thorncroft et al. 1993]. Figure 7 is constructed in a manner similar to that of Fig. 2: The QG^{+1} most unstable normal mode of base state (10) with $\mu = 1$, $\epsilon = 0.3$, and $A = -0.1$ is calculated first; the nonlinear QG^{+1} model is then initialized with that mode scaled so that $|\theta'(z = 0)|_{\max}$

= 0.20; the QG^{+1} base state and normal mode is also used as the initial condition for the companion PE integration; the QG integration is initialized with the QG base state ($\mu = 1$, $\epsilon = 0$, $A = -0.1$) and its most unstable normal mode. Davies et al. (1991), using a semigeostrophic model, showed that with $A = -0.1$ (using $\epsilon = 0.24$, and a baroclinic jet similar to the one shown in Fig. 1), there is an anticyclonic bias in the finite-amplitude wave pattern (see their Fig. 8). As shown in Fig. 7, this anticyclonic bias is evident in the QG, QG^{+1} , and PE solutions. It is also evident from Fig. 7 that, relative to the QG solution, the PE and QG^{+1} solutions are cyclonically biased. Of course with a cyclonically biased large-scale flow, there is a cyclonic bias even in the QG model, and the finite-Rossby-number tendency in both QG^{+1} and PE is to further accentuate this bias.

The similarity between the effects of horizontal shear and of dynamics beyond QG has been remarked upon previously in the literature (Snyder et al. 1991; Nakamura 1993). The QG^{+1} framework allows, for the first time, a direct explanation of this similarity. As illustrated by (15), (16) and Figs. 3 and 5, dynamics at the next order beyond QG include advections (of θ') by a flow that is qualitatively the same as the x -independent horizontal shear associated with nonzero A in the basic state (10). The key difference in these effects is that horizontal shear, being a modification to the basic state, acts linearly, while the asymmetric advections in QG^{+1} are nonlinear effects, in that they arise from quadratic nonlinearities in the PV inversion (5).

5. Conclusions

We have tested the numerical solution of the QG^{+1} equations (Muraki et al. 1999) against those of the primitive equations (PEs) for growing waves on a baroclinic jet. The QG^{+1} solutions improve upon the accuracy of QG in that they capture important mesoscale structure found in PE. Perhaps more important is the fact that QG^{+1} preserves the conceptual advantages of QG theory based on its analytical expression as the conservation and inversion of QG potential vorticity (PV). The ancillary QG concept of the \mathbf{Q} vector is directly incorporated into QG^{+1} since \mathbf{Q} appears as the forcing for the divergent-wind potentials [(6), (7)] so that frontogenetical feedbacks are explicitly included. These features also make QG^{+1} a potentially attractive tool for observational analysis on the mesoscale.

The present analysis of finite-amplitude baroclinic waves using QG^{+1} has shown the following.

- 1) The cyclonic bias in PE arises from the next-order correction in PV inversion, which in effect adds a cyclonic shear to base-state jet.
- 2) With the correct cyclonic bias, the QG^{+1} model produces the correct asymmetry in placement of the warm and cold fronts within the wave, and the cor-

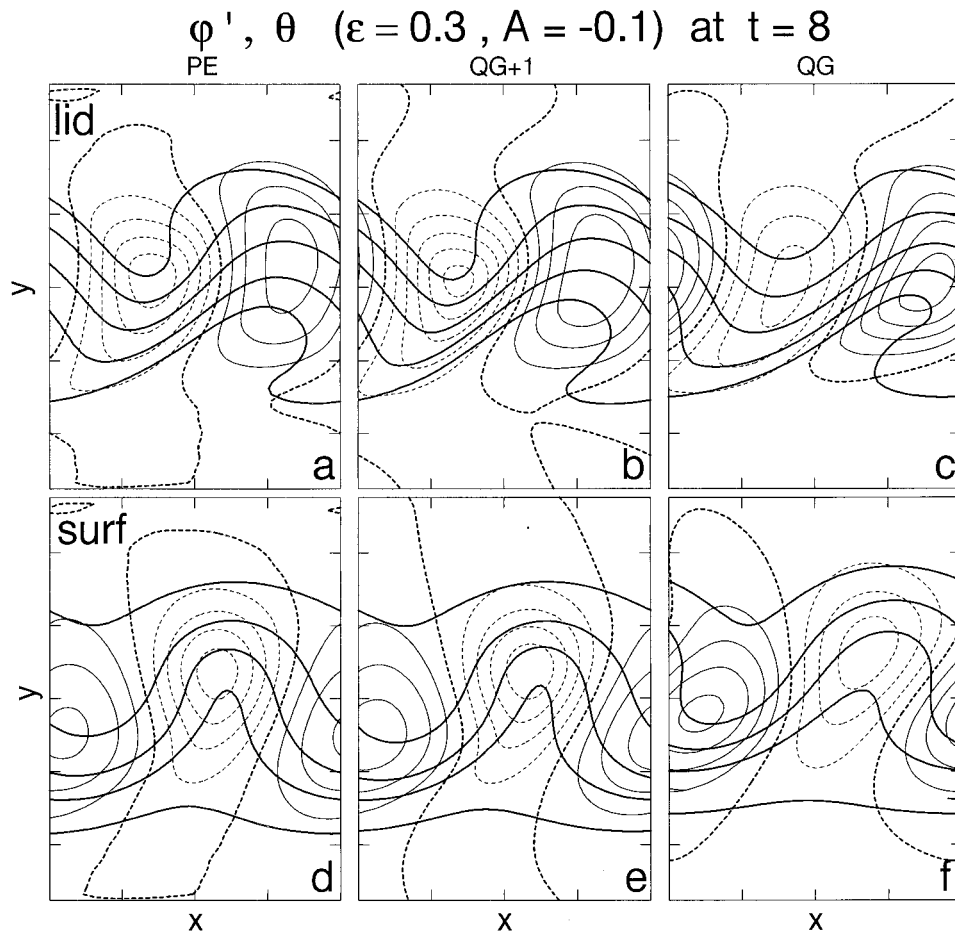


FIG. 7. As in Fig. 2 except with $A = -0.1$ and $t = 8$.

responding divergent-wind frontogenetical feedbacks.

- 3) As noted in the literature, anticyclonic or cyclonic bias may be induced in PE simulations of baroclinic waves through such bias in the base state. QG, QG⁺, and PE simulations shown here with an anticyclonically biased base state all show anticyclonic bias in the solutions—the QG⁺ and PE simulations show that, *relative to QG*, there is the finite-Rossby-number cyclonic bias identified in item 1).

The authors and collaborators are currently using the QG⁺ formalism described in MSR to study a variety of problems in mesoscale dynamics: QG⁺ is being used to extend the QG edge-wave analysis of waves on the tropopause (piecewise constant static stability, see, e.g., Rivest et al. 1992) to capture the observed asymmetry in vertical displacement between upper-level cyclones and anticyclones. QG⁺ is the natural model to extend the S(urface)QG study of Held et al. (1995) to higher order. This is because, as in SQG, the QG⁺ equations also can be reduced to a surface calculation and we have initiated an investigation into the asymmetrical organization of cyclonic and anticyclonic vortices from

small-scale initial conditions. Finally, as indicated in MSR, the restriction to balance dynamics does not follow directly from the formulation into QG⁺ potentials, but rather through the assumed asymptotic inversion scheme. An inversion scheme based upon a multiple space-scale asymptotic method (at small Rossby number), which incorporates gravity waves generated by flow over topography, is currently under development.

Acknowledgments. Thanks are due to C. Davis and G. Hakim of NCAR for their helpful comments on the first draft of this paper. DJM was supported through NSF DMR-9704724, DOE DE-FG02-88ER25053, and the Alfred P. Sloan Foundation.

APPENDIX

Numerical Solution of QG⁺

The set of dependent variables $\chi = \{q, \Phi, F, G, \phi\}$ are defined at $y_i = (i - 1)\Delta y$ ($i = 1, M + 1$), $x_k = (k - 1)\Delta x$ ($k = 1, L + 1$), and $z_j = (j - 0.5)\Delta z$ ($j = 1, N$) where $\Delta y = Y/M$, $\Delta x = X/L$, and $\Delta z = D/N$. The boundary temperatures, θ^s , are defined at (x_k, y_i) . The

dependent variables are decomposed as $\chi = \bar{\chi}(y, z) + \chi'(x, y, z, t)$, $\theta^s = \bar{\theta}^s(y) + \theta'^s(x, y, t)$. In the present study $D = 1$; $M = 64$, $L = 64$, and $N = 20$ for the main case study discussed in all figures except Fig. 3, which contains information from simulations using $M = 32$, $L = 32$, and $N = 10$.

The base state $(\bar{\chi}, \bar{\theta}^s)$ is obtained as follows. An x -independent solution $\Phi = \bar{\Phi}(y, z)$ immediately implies $\bar{F} = \bar{G} = 0$ by (6), (7) with $F^s = G^s = 0$; hence determination of an x -independent base state reduces to solution of (5). After separating out the nonperiodic-in- y part of $\bar{\Phi}$ and $\bar{\theta}^s$ with (10), the remaining task is to solve (11) under conditions (12). Equation (11) may be alternatively be expressed as

$$\begin{aligned} \bar{\Phi}_{yy} + \bar{\Phi}_{zz} = & -\epsilon[A\bar{\Phi}_{zz} + (2 - \mu)\bar{\Phi}_{yz} + (\bar{\Phi}_y\bar{\Phi}_{zz})_y \\ & - (\bar{\Phi}_y\bar{\Phi}_{yz})_z], \end{aligned} \quad (\text{A1})$$

and in second-order-accurate finite-difference form the latter is

$$\begin{aligned} (\delta_{yy} + \delta_{zz})\bar{\Phi} = & -\epsilon[A\delta_{zz}\bar{\Phi} + (2 - \mu)\delta_{yz}\bar{\Phi}^{yz} \\ & + \delta_y(\delta_y\bar{\Phi}\delta_{zz}\bar{\Phi}^y) - \delta_z(\delta_y\bar{\Phi}\delta_{yz}\bar{\Phi}^y)], \end{aligned} \quad (\text{A2})$$

where the standard notation $\delta_y\bar{\Phi} = [\bar{\Phi}(y + \Delta y/2) - \bar{\Phi}(y - \Delta y/2)]/\Delta y$ and $\bar{\Phi}^y = [\bar{\Phi}(y + \Delta y/2) + \bar{\Phi}(y - \Delta y/2)]/2$ has been used. The basic solution strategy is to solve (A2) with the $O(\epsilon)$ term set to zero to produce a first guess Φ_0 ; (A2) is then solved again for a corrected solution with the $O(\epsilon)$ terms computed using Φ_0 . At each step all that is required numerically is the solution of a Poisson equation. Since $(\bar{\Phi}, \bar{\theta}^s)$ are periodic-in- y , the Poisson equation is solved by taking the discrete Fourier transform in y of (A2) and (12) and then solving the resulting ordinary differential equations for the Fourier coefficients through inversion of a tridiagonal matrix.

With the base state $[\bar{\chi}(y, z), \bar{\theta}^s(y)]$ known, we solve the QG^{+1} equations for the horizontally periodic parts (χ', θ'^s) . The solution cycle begins with the inversion of an initially specified (q', θ'^s) for Φ' through solution of the equation

$$\begin{aligned} \nabla^2\Phi' = q' - \epsilon[& \bar{\Phi}_{yy}\Phi'_{zz} + (\Phi'_{xx} + \Phi'_{yy})\bar{\Phi}_{zz} - 2\bar{\Phi}_{yz}\Phi'_{yz} \\ & + (\Phi'_x\Phi'_{zz})_x - (\Phi'_x\Phi'_{xz})_z + (\Phi'_y\Phi'_{zz})_y \\ & - (\Phi'_y\Phi'_{yz})_z], \quad (\Phi'_z)^s = \theta'^s \end{aligned} \quad (\text{A3})$$

or in finite-difference form,

$$\begin{aligned} (\delta_{xx} + \delta_{yy} + \delta_{zz})\Phi' = & q' - \epsilon[\delta_{yy}\bar{\Phi}\delta_{zz}\Phi' + (\delta_{xx}\Phi' + \delta_{yy}\Phi')\delta_{zz}\bar{\Phi} \\ & - 2\delta_{yz}\bar{\Phi}\delta_{yz}\bar{\Phi}^{yz} + \delta_x(\delta_x\Phi'\delta_{zz}\bar{\Phi}^x) \\ & - \delta_z(\delta_x\bar{\Phi}'\delta_{xz}\bar{\Phi}^x) + \delta_y(\delta_y\Phi'\delta_{zz}\bar{\Phi}^y) \\ & - \delta_z(\delta_y\bar{\Phi}'\delta_{yz}\bar{\Phi}^y)], \end{aligned} \quad (\delta_z\Phi')^s = \theta'^s. \quad (\text{A4})$$

A first guess Φ'_0 is computed by setting the $O(\epsilon)$ term to zero in (A4); the corrected Φ' is obtained by solving (A4) again using Φ'_0 to compute the $O(\epsilon)$ terms. As with (A2) all that is required numerically at each step is the solution of a Poisson equation. The Poisson equation is solved by taking discrete Fourier transforms of (A4) in x and y and then solving the resulting ordinary differential equations for the Fourier coefficients through inversion of a tridiagonal matrix. Solvability of (A3) requires that

$$\int_V q' = \int_S [(1 + \epsilon\bar{\Phi}_{yy})\Phi'_z + \epsilon(\Phi'_{xx} + \Phi'_{yy})(\bar{\Phi}_z + \Phi'_z)]_{z=0}^{z=1}. \quad (\text{A5})$$

As discussed in section 4a of MSR, arbitrarily chosen (q', θ'^s) need not satisfy (A5), and so we do the following to initialize the model: we take the first pass at (A3) with $q' = 0$ and $\theta'^s = \theta(y)e^{ikx}$ so that solvability of (A3) for Φ'_0 is guaranteed by (A5) (with $\epsilon = 0$). In the second pass at (A3), solvability (A5) requires an $O(\epsilon)$ adjustment to q' , namely,

$$q'(0)V = \epsilon \int_S [(\Phi'_{0xx} + \Phi'_{0yy})\Phi'_{0z}]_{z=0}^{z=1}. \quad (\text{A6})$$

By virtue of the first of (1) and continuity, $\int_V q'(t) = q'(0)V$, and so any further solvability adjustments to $q'(t)$ required in the course of numerical solution are $O(\epsilon^2)$.

With Φ in hand, F and G are obtained by applying above-described Poisson-equation solution method to the finite-difference forms of (6), (7), namely,

$$\begin{aligned} (\delta_{xx} + \delta_{yy} + \delta_{zz})F = & 2\epsilon[-\delta_{yz}\bar{\Phi}^{yz}\delta_{xx}\Phi' + \delta_x(\delta_z\bar{\Phi}'\delta_{yz}\bar{\Phi}^{yz}) \\ & - \delta_y(\delta_z\bar{\Phi}'\delta_{xz}\bar{\Phi}^{yz})] \quad F^s = 0 \quad \text{and} \end{aligned} \quad (\text{A7})$$

$$\begin{aligned} (\delta_{xx} + \delta_{yy} + \delta_{zz})G = & 2\epsilon[\delta_{yy}\bar{\Phi}\delta_{yz}\bar{\Phi}^{yz} - \delta_{yz}\bar{\Phi}^{yz}\delta_{xy}\bar{\Phi}'^{xy} + \delta_x(\delta_z\bar{\Phi}'\delta_{yz}\bar{\Phi}^x) \\ & - \delta_y(\delta_z\bar{\Phi}'\delta_{xy}\bar{\Phi}^x)], \quad G^s = 0. \end{aligned} \quad (\text{A8})$$

Having obtained the potentials Φ , F , and G , the velocity field is constructed from the relevant elements of the finite-difference version of (3) and from (4) as

$$\begin{pmatrix} u \\ v \\ \epsilon w \end{pmatrix} = \begin{pmatrix} -\delta_y\bar{\Phi}^y - \delta_z\bar{F}^z \\ \delta_x\bar{\Phi}^x - \delta_z\bar{G}^z \\ \delta_x\bar{F}^x + \delta_y\bar{G}^y \end{pmatrix}. \quad (\text{A9})$$

With the velocity and (q, θ^s) known, (q, θ^s) is then updated through the finite-difference versions of (1). Using the second-order accurate leapfrog scheme, (1) becomes

$$\begin{aligned} \delta_t\bar{q}' = & -(u\delta_x\bar{q}' + v\delta_y\bar{q}' + \epsilon w\delta_z\bar{q}'), \\ \delta_t\bar{\theta}' = & -(u\delta_x\bar{\theta}' + v\delta_y\bar{\theta}'), \end{aligned} \quad (\text{A10})$$

where the rhs is evaluated at the middle time level (except for $t = 0$, when an Euler step is used). In the simulation shown in Fig. 2 and analyzed in Figs. 4–6, $\Delta t = 0.05$. The integrations used in the analysis of QG^{+1} error (Fig. 3) used $\Delta t = 0.02$ in order to match the smaller time step required in the companion PE solutions. In the present study only the second of (A10) was solved as our interest centered on cases with constant q .

Since $\bar{\Phi}$ is independent of x , (8) implies that $\bar{\phi} = \bar{\Phi}$; we obtained ϕ' for display in Fig. 2 from solution of the finite-difference form of (8)

$$\begin{aligned} & (\delta_{xx} + \delta_{yy} + \delta_{zz})(\phi' - \Phi') \\ &= 2\epsilon[\delta_{yy}\bar{\Phi}\delta_{xx}\Phi' + \delta_x(\delta_x\Phi'\delta_{yy}\bar{\Phi}'^x) \\ &\quad - \delta_y(\delta_x\bar{\Phi}'^{xy}\delta_{xy}\bar{\Phi}'^x)], \\ & [\delta_z(\phi' - \Phi')]^s = 0 \end{aligned} \quad (\text{A11})$$

by the Poisson-equation solution method already outlined.

REFERENCES

- Allen, J. S., and P. A. Newberger, 1993: On intermediate models for stratified flow. *J. Phys. Oceanogr.*, **23**, 2462–2486.
- , J. A. Barth, and P. A. Newberger, 1990: On intermediate models for barotropic continental shelf and slope flow fields. Part III: Comparisons of numerical model solutions in periodic channels. *J. Phys. Oceanogr.*, **20**, 1949–1973.
- Davies, H. C., C. Schär, and H. Wernli, 1991: The palette of fronts and cyclones within a baroclinic wave development. *J. Atmos. Sci.*, **48**, 1666–1689.
- Garnier, E., O. Metais, and M. Lesieur, 1998: Synoptic and frontal-cyclone scale instabilities in baroclinic jet flows. *J. Atmos. Sci.*, **55**, 1316–1335.
- Held, I. M., R. T. Pierrehumbert, S. T. Garner, and K. L. Swanson, 1995: Surface quasigeostrophic dynamics. *J. Fluid Mech.*, **282**, 1–20.
- Hoskins, B. J., 1975: The geostrophic momentum approximation and the semigeostrophic equations. *J. Atmos. Sci.*, **32**, 233–242.
- , and F. P. Bretherton, 1972: Atmospheric frontogenesis models: Mathematical formulation and solution. *J. Atmos. Sci.*, **29**, 11–37.
- , and N. V. West, 1979: Baroclinic waves and frontogenesis. Part II: Uniform potential vorticity jet flows—Cold and warm fronts. *J. Atmos. Sci.*, **36**, 1663–1680.
- , I. Draghici, and H. C. Davies, 1978: A new look at the ω -equation. *Quart. J. Roy. Meteor. Soc.*, **104**, 31–38.
- , M. E. McIntyre, and A. W. Robinson, 1985: On the use and significance of isentropic potential vorticity maps. *Quart. J. Roy. Meteor. Soc.*, **111**, 877–946.
- Mudrick, S. E., 1974: A numerical study of frontogenesis. *J. Atmos. Sci.*, **31**, 869–892.
- Muraki, D. J., C. Snyder, and R. Rotunno, 1999: The next-order corrections to quasigeostrophic theory. *J. Atmos. Sci.*, **56**, 1547–1560.
- Nakamura, N., 1993: Momentum flux, flow symmetry, and the nonlinear barotropic governor. *J. Atmos. Sci.*, **50**, 2159–2179.
- Polavarapu, S. M., and W. R. Peltier, 1990: The structure and nonlinear evolution of synoptic scale cyclones: Life cycle simulations with a cloud scale model. *J. Atmos. Sci.*, **47**, 2645–2672.
- Rivest, C., C. A. Davis, and B. F. Farrell, 1992: Upper-tropospheric synoptic-scale waves. Part I: Maintenance as Eady normal modes. *J. Atmos. Sci.*, **49**, 2108–2119.
- Rotunno, R., W. C. Skamarock, and C. Snyder, 1994: An analysis of frontogenesis in numerical simulations of baroclinic waves. *J. Atmos. Sci.*, **51**, 3373–3398.
- Smith, K. S., and G. K. Vallis, 1999: Linear baroclinic instability in extended regime geostrophic models. *J. Atmos. Sci.*, **56**, 1579–1593.
- Snyder, C., W. C. Skamarock, and R. Rotunno, 1991: A comparison of primitive-equation and semigeostrophic simulations of baroclinic waves. *J. Atmos. Sci.*, **48**, 2179–2194.
- Thorncroft, C. D., B. J. Hoskins, and M. E. McIntyre, 1993: Two paradigms of baroclinic-wave life-cycle behavior. *Quart. J. Roy. Meteor. Soc.*, **119**, 17–55.
- Whitaker, J. S., 1993: A comparison of primitive and balance equation simulations of baroclinic waves. *J. Atmos. Sci.*, **50**, 1519–1530.